
A PSYCHOPHYSICAL ORIENTED SALIENCY MAP PREDICTION MODEL

Qiang LI

Image Processing Laboratory, Parc Científic
University of Valencia
Valencia, 46980, Spain

qiang.li@uv.es

January 27, 2023

ABSTRACT

Visual attention is one of the most significant characteristics for selecting and understanding the visual redundancy of the external world. Complex scenes include enormous redundancy. The human vision system cannot process all information simultaneously, due to the visual information bottleneck. The human visual system mainly focuses on dominant parts of scenes, in order to reduce the redundant input of visual information. This is commonly known as visual attention prediction, or visual saliency map prediction. This paper proposes a new psychophysical saliency prediction architecture, WECSF, inspired by multi-channel model of visual cortex functioning in humans. The model consists of opponent color channels, a wavelet transform and wavelet energy map, and a contrast sensitivity function for extracting low-level image features and providing maximum approximation to the human visual system. In this paper, the proposed model is evaluated using several datasets, including the MIT1003¹, MIT300², TORONTO³, SID4VAM⁴, and UCF Sports datasets⁵, in order to demonstrate its efficiency. We also quantitatively and qualitatively compare the saliency prediction performance with that of other state-of-the-art models. Our model achieved stable and very good performance. Additionally, Fourier and spectral-inspired saliency prediction models outperformed other state-of-the-art non-neural network (and even deep neural network) models on psychophysical synthetic images. Finally, the proposed model can also be applied to spatial-temporal saliency prediction and achieved superior performance in the evaluation.

Keywords Visual attention · Redundancy · Multi-channel model · Opponent color channel · Wavelet energy map · Contrast sensitivity function · Saliency prediction

1 Introduction

Visual attention is a significant perceptive function in the human vision system (HSV), which is utilized to derive compact information from complex natural scenes [Treisman and Gelade, 1980]. Natural scene images contain a great amount of redundancy, which is generally useless for scene categories or recognition. Visual attention can extract essential features from redundant environments, benefiting visual information processing efficiency in the brain. The phenomenon of visual attention has been studied for a long time [Sun and Fisher, 2003]. Based on Barlow’s *efficiency coding hypothesis* [Barlow, 1959], visual attention is used to select relevant information and remove irrelevant

¹<http://people.csail.mit.edu/tjudd/WherePeopleLook/index.html>

²<http://saliency.mit.edu/>

³<http://www-sop.inria.fr/members/Neil.Bruce/>

⁴http://www.cvc.uab.es/neurobit/?page_id=53

⁵https://www.crcv.ucf.edu/data/UCF_Sports_Action.php

information from redundant vision scenes. In general, there are two types of visual attention mechanisms: Bottom-up and top-down. Bottom-up models are mainly stimulus-driven. They are used to extract image features, accompanied by visual information processing in the visual system (e.g., color, frequency, texture, orientation, and motion) [Wang et al., 2005]. In contrast, top-down approaches, which are goal-driven, usually involve high-level cognitive feedback and modulate low-level vision functions at a specific level [Itti, 2000]. In summary, both of the above computational neural models have been successfully applied to saliency map prediction.

Many studies have tried to carry out bottom-up or top-down computational modeling to predict saliency maps. One of the earliest classical computational models, proposed by Itti et al. [Itti et al., 1998], was based on bottom-up mechanisms. This model estimates the saliency map based on the human low-level vision system, where the model structure contains linear filtering, center-surround differences, across-scale combinations, and linear combinations. Achanta [Achanta et al., 2009] implemented a model for segmenting areas which produces high-resolution saliency maps to determine outstanding objects with clearly defined boundaries. Bruce and Tsotsos [Bruce and Tsotsos, 2005] suggested a model based on Shannon’s measurement of self-information for saliency. They applied this model in a neural system that demonstrated similar relations with the circuit in the primate visual cortex. Li et al. [Li et al., 2012] proposed a new bottom-up model for identifying visual saliency, based on the analysis of the amplitude spectrum of natural images. The saliency map was generated using the original phase and amplitude spectrum, in order to reconstruct the 2D signal and filter it to a selected scale by minimizing the saliency entropy. Hou and Zhang [Hou and Zhang, 2008] introduced a dynamic visual attention model based on the rarity of features. They measured each feature’s perspective entropy gain using the incremental coding length (ICL). Murray et al. [Murray et al., 2011] demonstrated that an effective color appearance model in human vision, which involves principled parameter selection as well as an innate spatial pooling function, can be extended to create a saliency model that outperforms state-of-the-art models. Zhang and Sclaroff [Zhang and Sclaroff, 2013] developed a new Boolean map-based saliency (BMS) model. The BMS model computes saliency maps by analyzing the topological structure of Boolean maps, based on the Gestalt principle of figure-ground segregation [Pinna et al., 2017]. Hou et al. [Hou et al., 2011] introduced a simple image descriptor known as the image signature. They established a saliency algorithm based on the image signature, in order to check if the estimated foreground overlaps with visually conspicuous image locations. Goferman [Goferman et al., 2010] presented a context-aware saliency method which attempts to detect image regions that represent the scene. This definition varies from previous definitions, in that its purpose is to detect the dominant object, rather than to identify fixation points. Hou and Zhang [Hou and Zhang, 2007] demonstrated a straightforward approach for detecting perceptual saliency in objects, which is unaffected by attributes, categories, or other types of prior information. They generate the corresponding saliency map in the spatial domain by evaluating an input image’s log-spectrum. Guo [Guo et al., 2008] proposed a fast and straightforward Fourier transform-based approach called spectral residual (SR), which uses the SR of the amplitude spectrum to generate the saliency map. Schauerte and Stiefelhagen [Schauerte and Stiefelhagen, 2012] proposed the use of eigenaxes and eigenangles for spectral saliency models based on a quaternion Fourier transform. Murray [Murray et al., 2013] proposed a saliency model based on a low-level spatiochromatic model, which successfully predicted chromatic induction phenomena [Otazu et al., 2010]. Riche [Riche et al., 2012] proposed a new bottom-up model of visual saliency. It uses a sequential bottom-up feature extraction process. Low-level features, including luminance and chrominance, are computed first, then medium-level features, such as image orientations, are derived from the data. Duncan’s integrated competition hypothesis was presented using a novel object-based visual attention model that extends SUN [Zhang et al., 2008], where two new processes in the proposed model were identified and studied in depth. The first process determines the visual salience of points and groupings, while the second employs hierarchical sorting. Seo and Milanfar [Seo and Milanfar, 2009] presented a novel unified framework for detecting both static and spatial-temporal saliency. The “self-resemblance” calculation is then used to determine visual saliency. Spratling [Spratling, 2011] proposed a saliency prediction model based on predictive coding theory, which is a subset of the predictive coding theory that has previously been shown to account for the response properties of orientation-tuned cells in the primary visual cortex (V1) [Spratling, 2016]. As a result, this model offers a possible implementation of the hypothesis that V1 generates a bottom-up saliency map. Moreover, wavelet transforms have also begun to be used to estimate computational vision saliency maps [Murray et al., 2011]. Compared to the Fourier transform, it has a high resolution in both the frequency and time domains. Wavelet transforms can decompose signals at different scales, also known as multi-resolution/multi-scale analysis or sub-band coding, which can capture more low-level features from the original signal [Louis et al., 1997]. On the other hand, the wavelet transform approach can explain the primary visual cortex (V1) properties and produce multi-scale and multi-orientation features when provided stimuli. The final estimated saliency map sums up all the processed wavelet coefficients through an inverse wavelet transform [Selvaraj and Shebiah, 2009]. The shortcomings of wavelet transform saliency maps include a loss of global contrast information, rather than local contrast information.

In the last few years, some studies have attempted to estimate saliency maps with deep convolutional neural networks (CNNs), which have achieved impressive performances compared to conventional methods [Borji, 2019, Kruthiventi et al., 2016]. Cornia et al. [Cornia et al., 2016] introduced a novel deep architecture for saliency prediction. To predict

Model	Author(s)	Year	Inspiration
ITII	[Itti et al., 1998]	1998	Biological
Achanta	[Achanta et al., 2009]	2009	Fourier/Spectral
AIM	[Bruce and Tsotsos, 2005]	2005	Biological/Information-Theoretic
HFT	[li et al., 2012]	2013	Fourier/Spectral
ICL	[Hou and Zhang, 2008]	2008	Information-Theoretic
SIM	[Murray et al., 2011]	2011	Biological
BMS	[Zhang and Sclaroff, 2013]	2013	Probabilistic
DCTS	[Hou et al., 2011]	2011	Fourier/Spectral
CASD	[Goferman et al., 2010]	2010	Biological/Probabilistic
PFT	[Hou and Zhang, 2007]	2007	Fourier/Spectral
PQFT	[Guo et al., 2008]	2008	Fourier/Spectral
QDCT	[Schauerte and Stiefelhagen, 2012]	2012	Fourier/Spectral
SIMgrouping	[Murray et al., 2013]	2013	Biological/Cognitive
RARE	[Riche et al., 2012]	2012	Information-Theoretic
SUN	[Zhang et al., 2008]	2008	Probabilistic
SeoMilanfar	[Seo and Milanfar, 2009]	2009	Biological/Cognitive
Spratling	[Spratling, 2011]	2011	Biological/Cognitive
Simpsal	[Harel, 2012]	2012	Biological/Cognitive
ML_Net	[Cornia et al., 2016]	2016	Biological/Deep Neural Network
DeepGazeII	[Kümmerer et al., 2016]	2016	Biological/Deep Neural Network

Table 1: Saliency prediction models. The model function categories that inspired the developed corresponding models are shown on the right side of the table. Most saliency prediction models were inspired by biological/cognitive, Fourier/spectral, information-theoretic, and probabilistic principles.

saliency maps, current state-of-the-art models for saliency prediction use fully convolutional networks, which utilize a non-linear combination of features extracted from the last convolutional layer. DeepGazeII [Kümmerer et al., 2016] is a model which forecasts where people will look in images. The model employs features from the VGG-19 deep neural network, which has been trained to recognize objects in images. Compared to conventional methods, deep learning implementations are easier to transfer to real-life applications, such as object detection, video understanding, and image compression. All of the aforementioned saliency prediction models are listed in Tab. 1.

In this study, we propose a saliency prediction model inspired by the low-level human vision cortex. The model contains opponent color channel, wavelet energy map, and contrast sensitivity function (CSF) components, in order to predict human visual attention. The proposed model is a bottom-up model, and it was evaluated using certain metrics, including the area under the ROC curve (AUC) [Borji et al., 2013], normalized scanpath saliency (NSS) [Emami and Hoberock, 2013], Pearson’s correlation coefficient (CC) [Engelke et al., 2012], similarity intersection (SIM) [Riche et al., 2013], Kullback–Leibler divergence (KL) [Wilming et al., 2011], and information gain (IG) [Kümmerer et al., 2015b]. The details of these metrics will be introduced in Section 3. The proposed model was quantitatively evaluated using the MIT1003, TORONTO, and SID4VAM datasets, in comparison with other models.

The rest of this paper is organized as follows: Section 2 introduces the concepts of opponent color space, wavelet decomposition, wavelet energy map estimation, and CSF. Section 3 introduces the saliency map prediction model, along with different datasets and evaluation metrics. Section 4 presents the experimental results. The final section provides discussions and conclusions for the paper.

2 The Proposed Saliency Prediction Model

2.1 Saliency Prediction Model

In this paper, we propose a biologically inspired visual saliency prediction map, based on the human low-level visual system. The extraction of information in the retina, LGN, and V1 are critical components of visual neural networks. The color opponent channel, wavelet transform, wavelet energy map, and contrast sensitivity function are the main components of the proposed model architecture. The color opponent channel simulates the response of retinal cells to different spectral wavelengths, and the wavelet transform presents the multi-scale and multi-orientation properties of the V1. The CSF is used to describe the human brain’s susceptibility to spatial frequencies. The details of each component are described in the following sections. The computational saliency prediction model architecture is illustrated in Fig. 1.

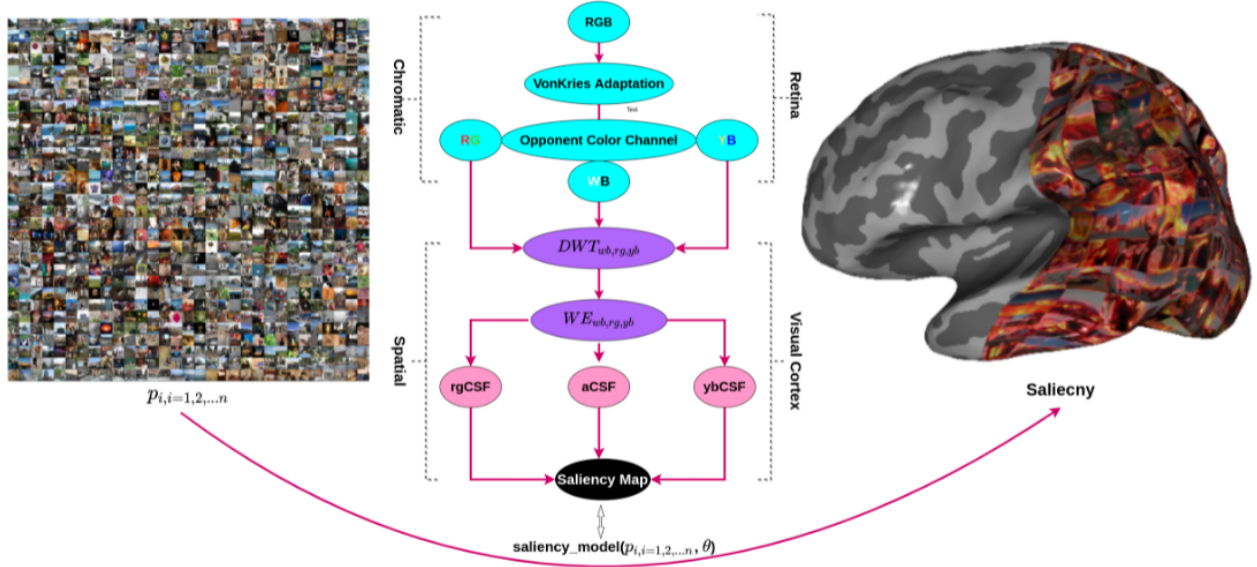


Figure 1: Architecture of the proposed saliency prediction model. The left panel image was selected from the MIT1003 dataset. The flow chart shows the framework of the proposed model, containing the chromatic response in the retina and spatial feature processing in the visual cortex. The natural image is first adapted, before decomposing it into white–black, red–green, and yellow–blue opponent neural channels. In the spatial component, a discrete wavelet transform is applied to each opponent color channel, then the wavelet energy map is measured. In the last step of the proposed model, the CSF is applied to each opponent wavelet energy channel and combined with each opponent’s feature. i and θ indicate image and model parameters, respectively. The details of each component are described in the following section. The graph on the right refers to the map of the left panel image’s saliency on the inflated visual cortex using the proposed model.

2.2 Gain control with von Kries chromatic adaptation model

Gain control theory has been widely used in cognitive psychology, and is closely related to human dynamic behavior [Mercy, 1981]. Gain control exists in the visual information processing pipeline in the retina and cortex. In other words, gain control affects top-down and bottom-up visual information flows, as well as attention-related cognitive functioning [Butz, 2004]. Meanwhile, the gain control always strives to maintain a steady-state brain and self-regulation condition between the brain and the natural environment. In the von Kries model, we multiply each channel of the image with the gain value after normalizing its intensity [Finlayson et al., 1993, 2002, Krauskopf and Gegenfurtner, 1992]. However, there are some implications to this approach. The first is that the channels are considered independent signals, which is why we use independent gains. Second, this gain is added not in the RGB space but, instead, the tristimulus LMS space. Assuming that the LMS corresponds to the tristimulus values of our image, the von Kries model can be mathematically expressed as:

$$L_2 = \frac{L_1}{L_{\max}} L_{\max 2}, M_2 = \frac{M_1}{M_{\max}} M_{\max 2}, S_2 = \frac{S_1}{S_{\max}} S_{\max 2}, \quad (1)$$

$$\begin{bmatrix} L_{\text{post}} \\ M_{\text{post}} \\ S_{\text{post}} \end{bmatrix} = \begin{bmatrix} \frac{1}{L_{\max}} & 0 & 0 \\ 0 & \frac{1}{M_{\max}} & 0 \\ 0 & 0 & \frac{1}{S_{\max}} \end{bmatrix} \begin{bmatrix} L_1 \\ M_1 \\ S_1 \end{bmatrix}, \quad (2)$$

$$\begin{bmatrix} L_2 \\ M_2 \\ S_2 \end{bmatrix} = \begin{bmatrix} L_{\max 2} & 0 & 0 \\ 0 & M_{\max 2} & 0 \\ 0 & 0 & S_{\max 2} \end{bmatrix}, \quad (3)$$

where L_1 corresponds to the original image’s L values; L_{\max} , M_{\max} , and S_{\max} , respectively, correspond to the maximum value of each channel in the LMS image; $L_{\max 2}$, $M_{\max 2}$, and $S_{\max 2}$ are the gain values with a set value of 0.6 in the proposed model; and L_2 is the corrected L channel after adaptation.

2.3 Color Appearance Model

The color opponent channel in the proposed model is described in this section. Representation of color in the brain can improve object recognition and identity, while also reducing redundancy. As previously stated, visual information input from the natural environment contains significant redundancy [Barlow, 1990]. Trichromatic theory [Brill, 2014] and the proposed color appearance model, inspired by the functioning of the low-level human visual system, help us to understand how the sensors encode color information and have been widely used in low-level image processing. Two functional types of chromatic sensitivity or selectivity sensors were found—single-opponent and double-opponent neurons—based on the responses of long (L), mediate (M), and short (S) cones in the physical world [Shapley and Hawken, 2011] (see Fig. 2).

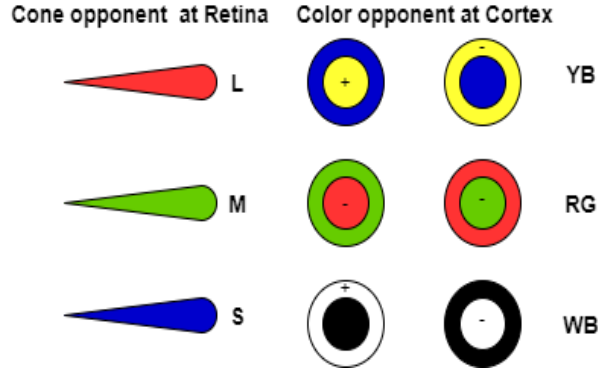


Figure 2: The receptive field of opponent color channels in the retina and visual cortex. L, M, and S refer to long, mediate, and short cones in the retina; YB, RG, and WB indicate yellow–blue, red–green, and white–black opponent color channels, respectively. "+" indicates excitation, "-" represents inhibition.

Most saliency prediction models use CIELAB and YUV color spaces for the opponent color spaces. In our case, we introduce a new opponent color space, proposed by Hering in 1957 [Hurvich and Jameson, 1957]. The color space transform matrix from RGB to $O_1O_2O_3$ can be expressed as:

$$\begin{bmatrix} O_1 \\ O_2 \\ O_3 \end{bmatrix} = \begin{bmatrix} 0.2814 & 0.6938 & 0.0638 \\ -0.0971 & 0.1458 & -0.0250 \\ -0.0930 & -0.2529 & 0.4665 \end{bmatrix} \begin{bmatrix} R \\ G \\ B \end{bmatrix}. \quad (4)$$

The test natural scene images (of sizes 256×256 and 512×512) were selected from the Signal and Image Processing Institute, University of Southern California⁶, and the Kodak lossless true-color image database⁷ (of sizes 512×768 , 768×512 , and 768×512). The total natural color images were resized into the same size (8 bits, 256×256) as test images. All natural chromatic images were converted from RGB space to the ATD domain, based on the above conversion matrix. As can be seen in Fig. 3, the chromatic information (white–black, red–green, and yellow–blue) was decomposed into each channel.

⁶<http://sipi.usc.edu/database/database.php?volume=misc>

⁷<http://r0k.us/graphics/kodak/>

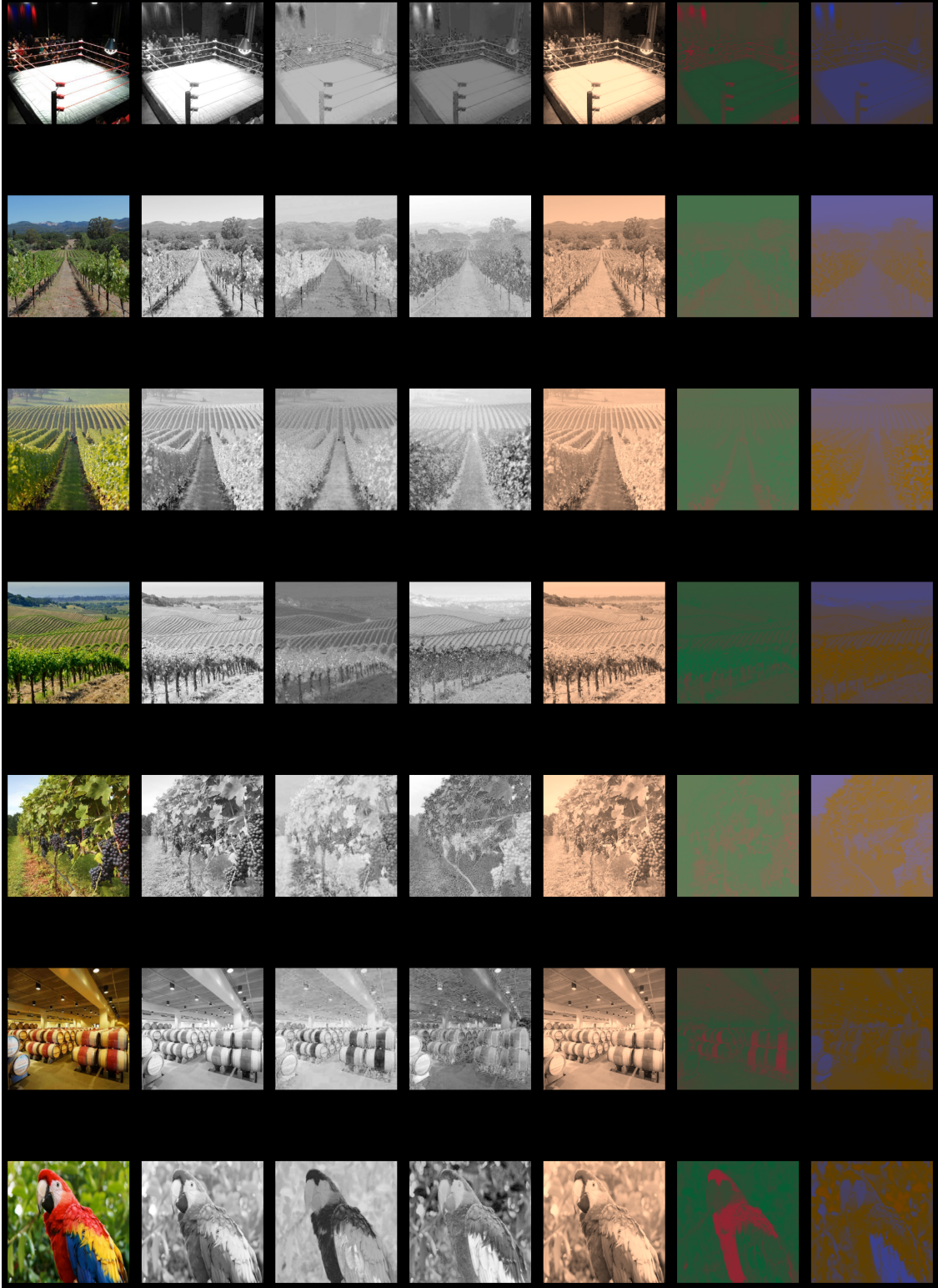


Figure 3: Opponent color processing. The first column represents the raw RGB color space, followed by the white–black (WB) channel, red–green (RG) channel, and yellow–blue (YB) channel, each with a gray colormap. The final three columns depict the WB, RG, and YB channels in artificial color, in order to better visualize the opponent color processing at the visual cortex level.

2.4 Wavelet Energy Map

2.4.1 Visual cortex receptive fields with wavelet filters

The primary visual cortex contains neurons that reflect the structure of the retinal image, in terms of a wavelet basis, and the visual simple and complex cells can be modeled with wavelet filters. In our case, we did not consider the in-depth details of each hypercolumn neuron's interaction mechanisms (e.g., Li's model [Zhaoping, 1998]). The simulated V1 complex receptive fields sum all the squares of different scales and orientations after the wavelet transform (see Fig. 4). The V1 simple receptive fields in each opponent channel are mathematically defined as:

$$V_{iv} = s_i o_v \quad (5)$$

$$V_{ih} = s_i o_h \quad (6)$$

$$V_{id} = s_i o_d, \quad (7)$$

where s indicates receptive field scales, o refers to orientation—that is, vertical (v), horizontal (h), and diagonal (d)—and i indicates the number of neurons/features. The V1 complex cells can be formulated as:

$$V_{complex} = \sum_1^i (s_i o_v)^2 + \sum_1^i (s_i o_h)^2 + \sum_1^i (s_i o_d)^2. \quad (8)$$

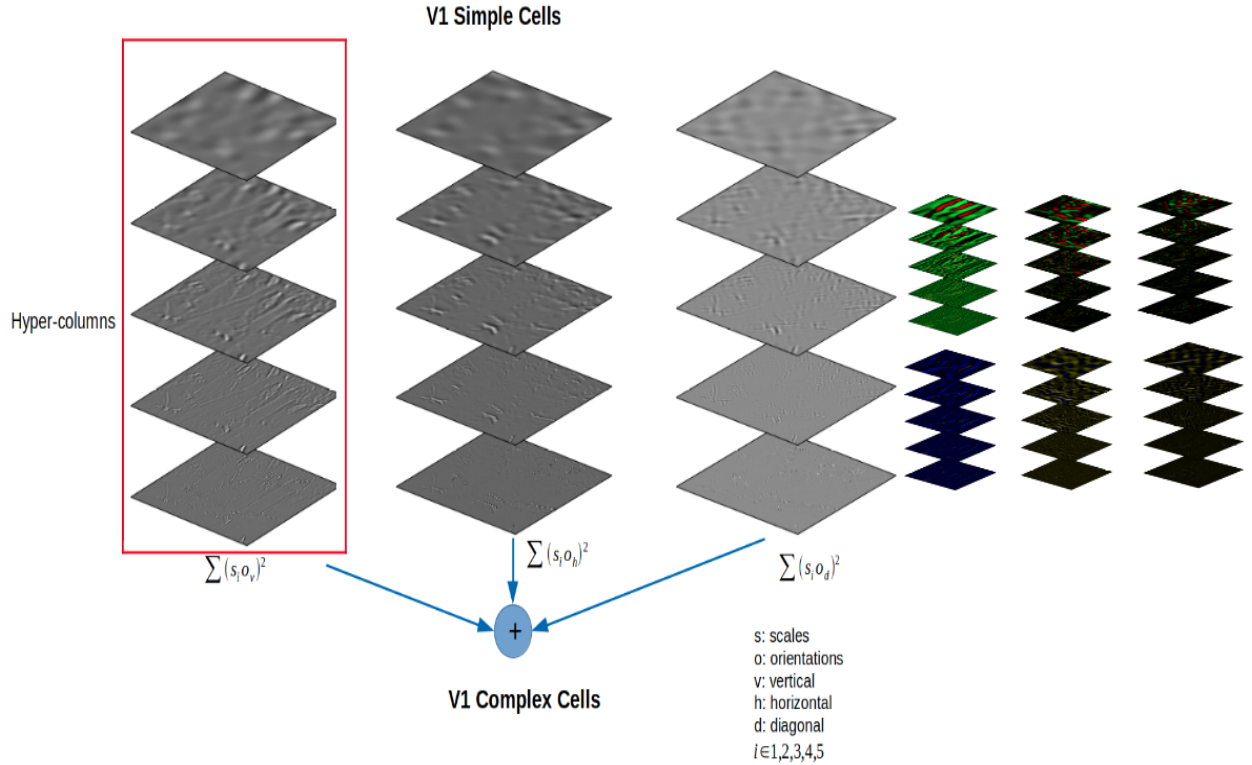


Figure 4: The modeling of V1 simple and complex cells in each opponent channel. The red rectangle indicates hypercolumns in the visual cortex. From left to right, the graph depicts WB opponent neurons with different orientations and scales. The following zoomed out top/bottom graphs with artificial color, for better visualization of features, in each hypercolumn indicate RG/YB opponent neurons across different orientations and scales. The V1 complex cells can be obtained from the sum of squares of wavelet transform features across scales and orientations in the simple cells.

2.4.2 Wavelet transform and wavelet energy map

The wavelet image analysis can decompose an image into multi-scale and multi-orientation features, similar to the visual cortex representation. Compared to the Fourier transform (FT), a wavelet transform can represent spatial and frequency information simultaneously. Alfred Haar first proposed the wavelet transform approach, and it has already been widely used in signal analysis [Haar, 1912]; for example, for image compression, image denoising, and classification. Wavelet transforms have already been applied in visual saliency map prediction, and achieved good performance [imamoğlu et al., 2013]. However, wavelet energy maps remain barely used in visual saliency map prediction, and they can be used to enhance local contrast information in the decomposition sub-bands. A discrete wavelet transform (DWT) is used in our proposed model, which can be mathematically expressed as:

$$r[n] = ((I * f)[n]) \downarrow 2 = \left(\sum_{k=-\infty}^{\infty} I[k]f[n-k] \right) \downarrow 2 \quad (9)$$

where I indicates the input images, f represents a series of filter banks (low-pass and high-pass), and $\downarrow 2$ indicates down-sampling until the next layer's signal cannot be decomposed any more (see Fig. 5). A series of sub-band images are produced after convolution with the DWT; then, the wavelet energy map can be calculated from each sub-band feature (see Fig. 6).

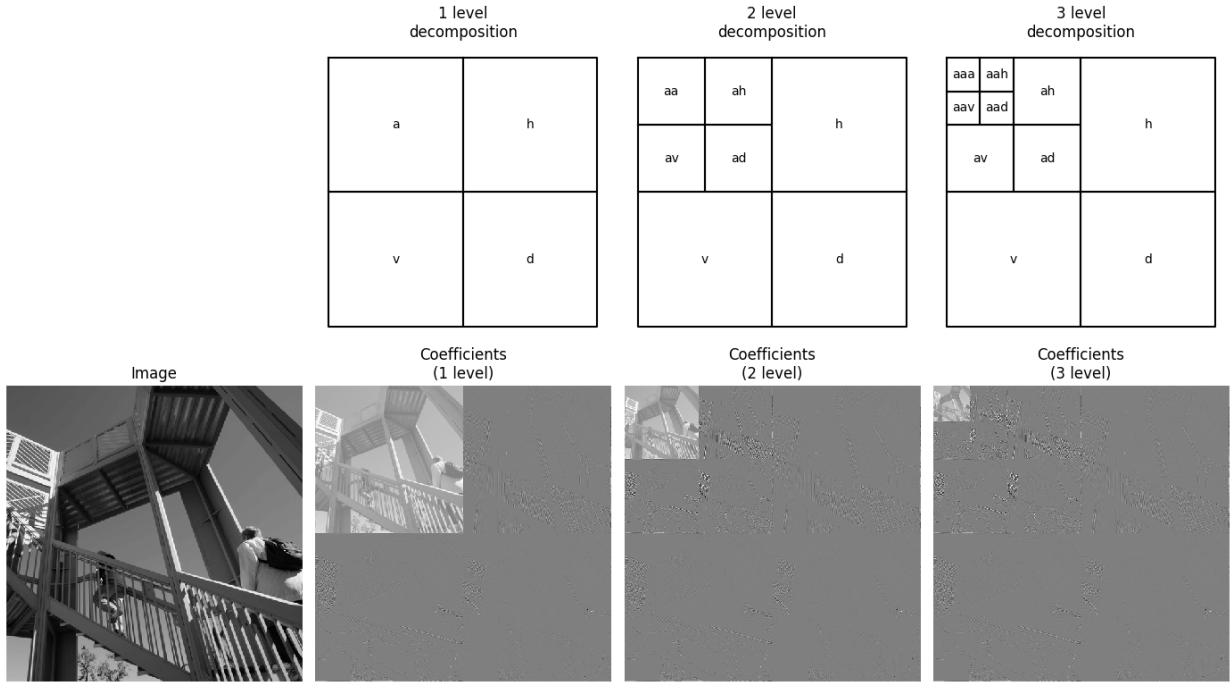


Figure 5: The different decomposition levels of the DWT (e.g., first, second, and third levels): “a” indicates the original image, “h” indicates the horizontal feature, “v” refers to the vertical feature, and “d” represents the diagonal feature. The bottom-left image is the original image, and the following images represent the first-, second-, and third-level decomposition features from the original image.

The wavelet energy map can be expressed as:

$$\mathcal{WE}(i, j) = \|I(i, j)\|^2 = \sum_{k=1}^{3ind+1} |I_k(i, j)|^2, \quad (10)$$

where ind indicates the maximum level of an image that can be decomposed in the last level, and $I_k(i, j)^2$ represents the energy map of each sub-band feature.

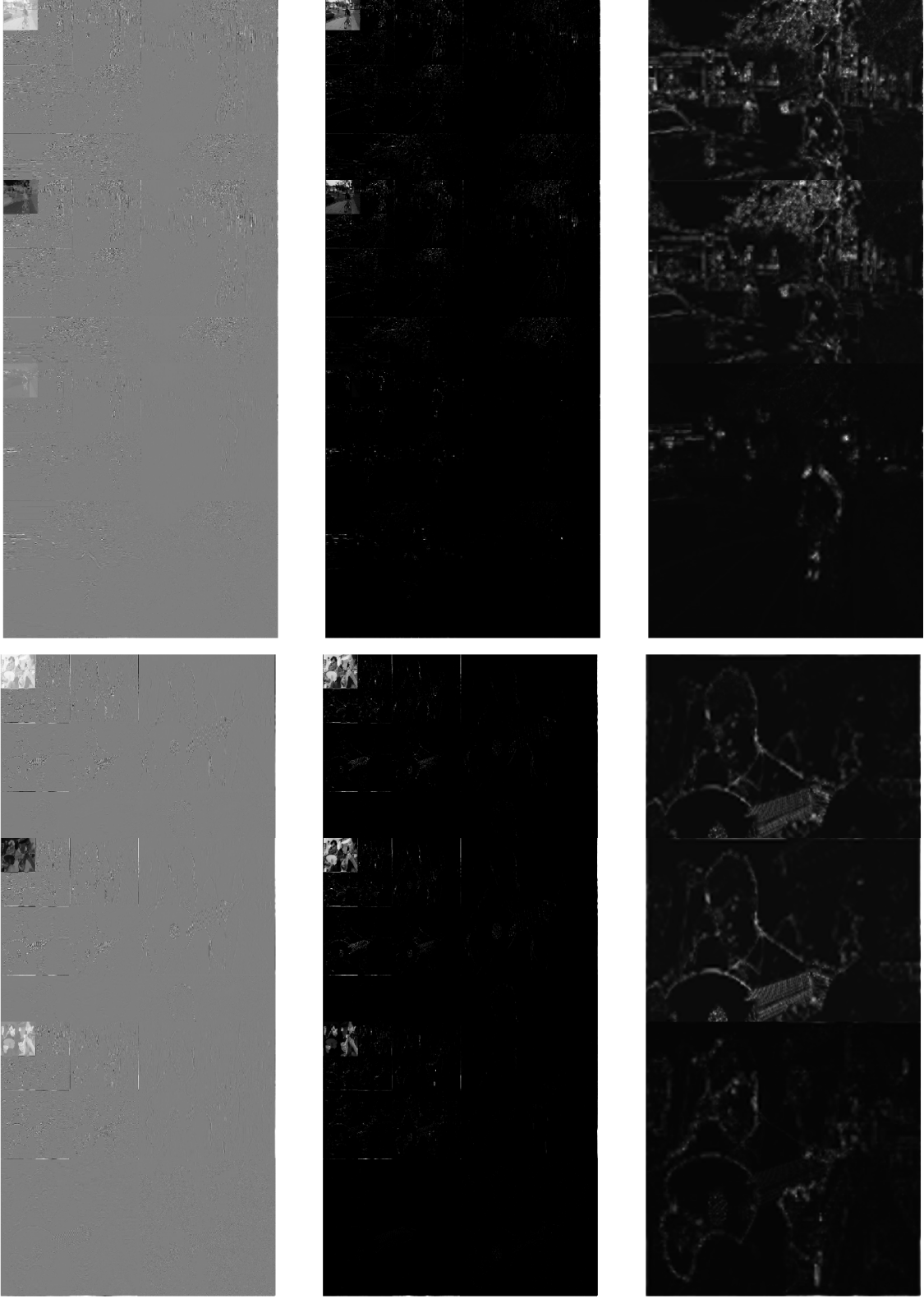


Figure 6: Each channel’s DWT map and the wavelet energy maps corresponding to it. The first column shows the DWT maps for achromatic (WB) and chromatic (RG, YB) channels. The second column is the wavelet energy map, obtained by summing across scales and orientation features for WB, RG, and YB opponent channels, respectively. The last column shows the sum of squares energy maps in each opponent channel.

2.5 Contrast Sensitivity Function

The human visual system is sensitive to contrast changes in natural environments. The visual cortex function can be decomposed into subset compositions, where one of the significant features is the CSF, which can be divided into achromatic and chromatic spatial CSFs [Mullen, 1985]. In this proposed computational model, an achromatic CSF (aCSF) and chromatic CSFs (rgCSF and ybCSF) were implemented, which was first proposed by Mannos and Sakrison in 1974 [Mannos and Sakrison, 1974], and further improved later [Watson and Malo, 2002, Watson and Ahumada, 2010] (see Fig. 7). The achromatic CSF mathematics can be expressed as:

$$\text{CSF}(f_x, f_y) = Q(f) * L(f_x, f_y), \quad (11)$$

$$Q(f) = g * (\exp(-(f/f_m)) - l * \exp(-(f^2/s^2))), \quad (12)$$

$$L(f_x, f_y) = 1 - w * (4(1 - \exp(-(f/os))) * f_x^2 * f_y^2 / f^4), \quad (13)$$

where (f_x, f_y) indicates a 2D spatial frequency vector (in cycle/deg), f represents the modulus of the spatial frequency (cycle/deg), g represents the overall gain ($g = 330.74$), f_m is a parameter that controls the exponential decay of the CSF Tyler ($f_m = 7.28$), l represents the loss at low frequencies ($l = 0.837$), s is a parameter that controls the attenuation of the loss factor at high frequencies ($s = 1.809$), w indicates the weighting of the oblique effect ($w = 1$), and os indicates the oblique effect scale ($os = 6.664$).

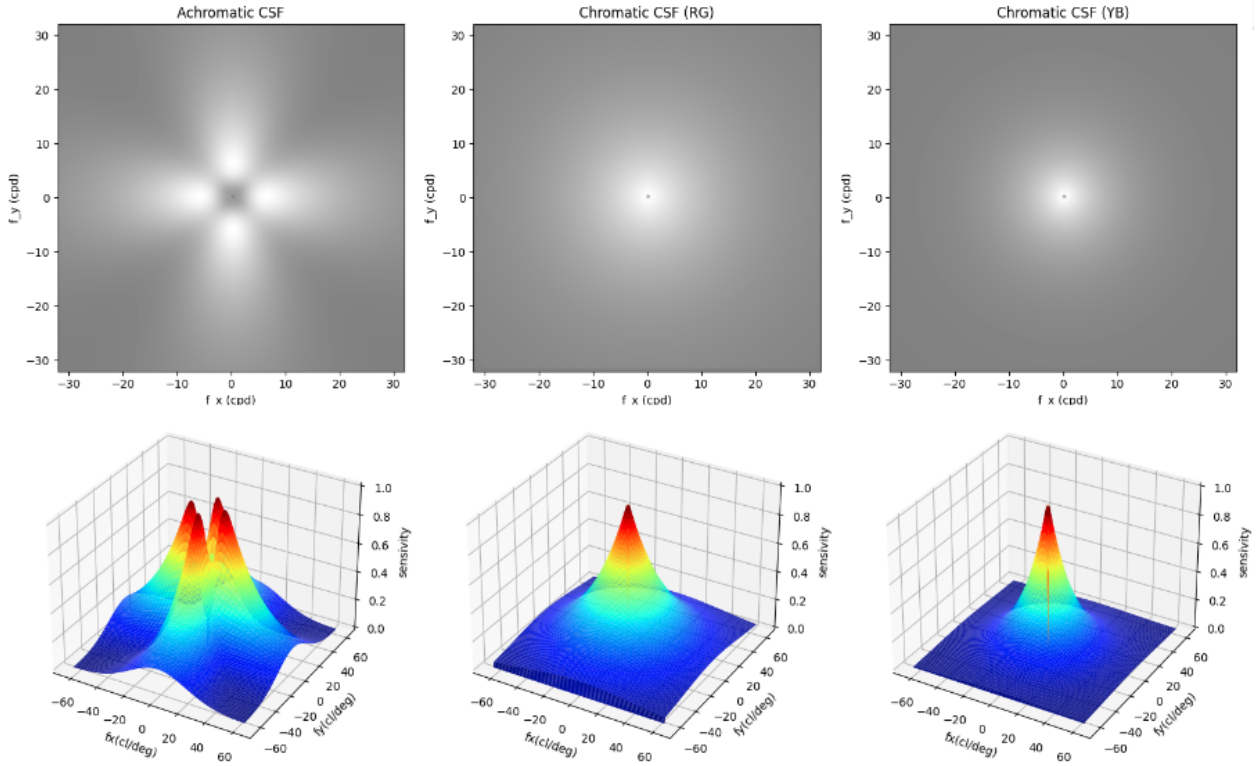


Figure 7: Achromatic and chromatic CSFs. The images in the top row are 2D CSFs, and the bottom row shows 3D CSFs.

The CSFs were applied to the wavelet energy image in the Fourier domains. It can be described by the following formula:

$$CSF_{WE} = \text{real}(\mathcal{F}(\mathcal{I}(\mathcal{F}(WE.\text{real})) \otimes CSF))), \quad (14)$$

where \mathcal{F} indicates the 2D Fourier transform, \mathcal{F} indicates the 2D inverse Fourier transform, \mathcal{I} indicates *fftshift*, and \mathcal{I} indicates *ifftshift*. The Python implementations of the above CSFs (aCSF, rgCSF, and ybCSF) are available at <https://github.com/sinodanishspain/CSFpy>.

3 Materials and Methods

3.1 datasets

The proposed model was tested on several well-known datasets, including MIT1003, MIT300, TORONTO, and SID4VAM. The basic information of each dataset is introduced in the following subsections.

3.1.1 MIT1003

MIT1003 is an image dataset that includes 1003 images from the Flickr and LabelMe collections (see Fig. 8). The fixation map was generated by recording the eye-tracking data of 15 participants. It is the largest eye-tracking dataset. The dataset includes 779 landscape and 228 portrait images with sizes spanning from 405×405 to 1024×1024 pixels [Judd et al., 2012].

3.1.2 MIT300

MIT300 is a benchmark saliency test dataset that includes 300 images obtained by recoding a 39-observer eye-tracking dataset (see Fig. 8). The MIT300 dataset categories are highly varied and natural. The dataset can be used for model evaluation [Judd et al., 2012].



Figure 8: MIT1003 (left panel image) and MIT300 (right panel image) datasets.

3.1.3 TORONTO

The TORONTO dataset includes 120 chromatic images free-viewed by 20 subjects (see Fig. 9). The dataset contains both outdoor and indoor scenes with a fixed resolution of 511×681 pixels [Bruce and Tsotsos, 2005].

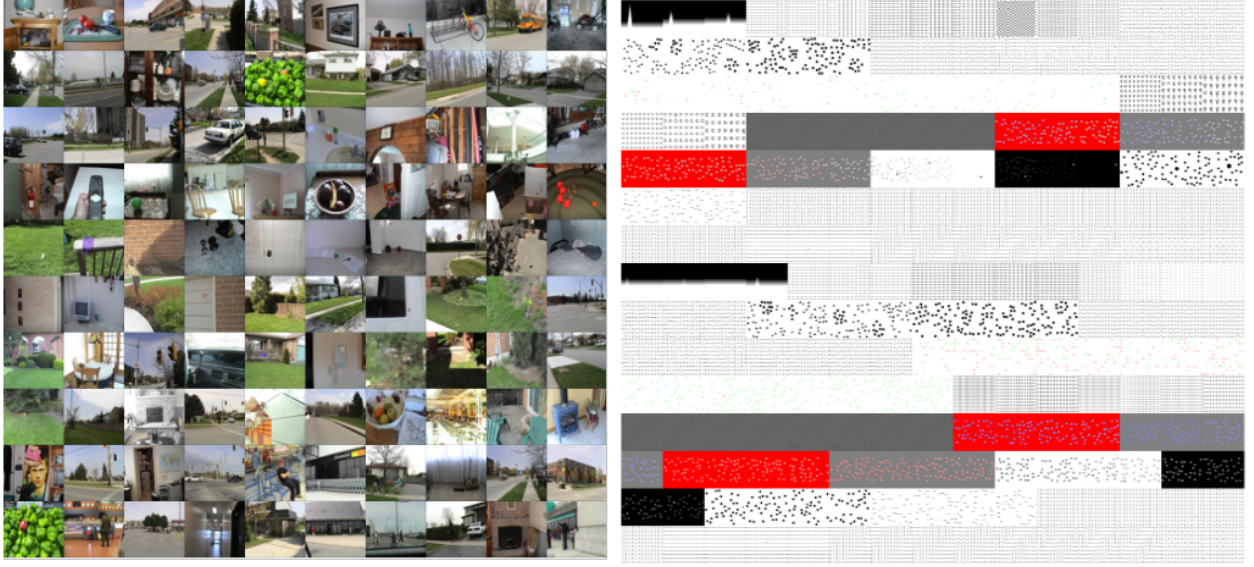


Figure 9: TORONTO (left) and SID4VAM (right) datasets.

3.1.4 SID4VAM

SID4VAM is a synthetic image database that is mainly used to psychophysically evaluate the V1 properties (see Fig. 9). This database is composed of 230 synthetic images, including 15 distinct types of low-level features (e.g., brightness, size, color, and orientation) with different target-distractor pop-out-type synthetic images [Berga et al., 2019].

3.2 Evaluation Metrics

There are several approaches, as mentioned before, to evaluate metrics between visual saliency and model prediction. In general, saliency evaluation can be divided into two branches: location- and distribution-based. The former mainly focuses on the district located in the saliency map, and the latter considers both the predicted saliency and human eye fixation maps as continuous distributions [Bylinskii et al., 2016]. In this research, we used AUC, NSS, CC, SIM, IG, and KL to evaluate the methods and details of each evaluation metric, as described in the following⁸.

3.2.1 Area under the ROC Curve (AUC)

The AUC metric is a popular approach for the evaluation of saliency model performance. The saliency map can be treated as a binary classifier to split positive samples from negative samples by setting different thresholds. The true positive (TP) is the proportion of saliency map values beyond a specific threshold at the fixation locations. In contrast, the false positive (FP) is the proportion of saliency map values beyond a specific threshold at the non-fixation locations. In our case, the thresholds were set from the saliency map values and the AUC-Judd, AUC-Borji, and sAUC measures [Borji et al., 2013].

3.2.2 Normalized Scanpath Saliency (NSS)

The NSS metric usually measures the relationship between human eye fixation maps and model-predicted saliency maps [Emami and Hoberock, 2013]. Given a binary fixation map F and saliency map S , the NSS can be formally defined as:

$$NSS = \frac{1}{N} \sum_{i=1}^N \bar{S}(i) \times F(i), \quad (15)$$

⁸<https://github.com/cvzoya/saliency>

$$N = \sum_i F(i) \text{ and } \bar{S} = \frac{S - \mu(S)}{\sigma(S)}, \quad (16)$$

where N is the total number of human eye positions, $\mu(s)$ is the mean value of saliency maps, and $\sigma(S)$ is the standard deviation.

3.2.3 Similarity Metric (SIM)

The similarity metric (SIM) is a very famous algorithm for measuring image structure similarity, which has already been widely used in image quality and image processing disciplines [Riche et al., 2013]. The SIM mainly measures the normalized probability distributions of eye fixation and model-predicted saliency maps. The SIM can be mathematically described as:

$$SIM = \sum_{i=1} \min(P(i), Q(i)), \quad (17)$$

where $P(i)$ and $Q(i)$ are the normalized saliency map and the fixation map, respectively. A similarity score should be in the range between zero and one.

3.2.4 Information Gain (IG)

The information gain is an approach to measuring saliency map prediction accuracy from an information-theoretic view. It mainly measures the critical information contained in the predicted saliency map, compared with a ground-truth map [Kümmerer et al., 2015a]. The mathematical formula for the IG can be expressed as:

$$IG(P, Q^B) = \frac{1}{N} \sum_i Q_i^B [\log_2(\epsilon + P_i) - \log_2(\epsilon + B_i)], \quad (18)$$

where P indicates the predicted saliency map, Q^B is the baseline map, and ϵ represents a regularity parameter.

3.2.5 Pearson's Correlation Coefficient (CC)

Pearson's correlation coefficient (CC) is a linear approach that measures how many similarities there are between the predicted saliency map and the baseline map [Jost et al., 2005].

$$CC(P, Q^D) = \frac{\sigma(P, Q^D)}{\sigma(P) \times \sigma(Q^D)}, \quad (19)$$

where P indicates the predicted saliency map and Q^D is the ground-truth saliency map.

3.2.6 Kullback–Leibler divergence (KL)

The Kullback–Leibler divergence (KL) is used to measure the distance between the samples of two distributions from an information-theoretic perspective [Kümmerer et al., 2015a]. It can be formally defined as:

$$KL(P, Q^D) = \sum_i Q_i^D \log \left(\epsilon + \frac{Q_i^D}{\epsilon + P_i} \right), \quad (20)$$

where P indicates the predicted saliency map, Q^D is the ground-truth saliency map, and ϵ represents a regularity parameter.

3.2.7 Other metrics

We also evaluated the performance of different salient prediction models through two main metrics: precision–recall curves (PR curves) and the F-measure⁹. By binarizing the predicted saliency map with thresholds in [0,255], a series of

⁹https://github.com/ArcherFMY/sal_eval_toolbox/

precision and recall score pairs was calculated for each dataset image. The PR curve was plotted using the average precision and recall of the dataset under different thresholds [Feng, 2018].

4 Experimental Results

4.1 Quantitative Comparison of the Proposed Model with other State-of-the-Art Models

To evaluate the performance of the proposed model, we compared it with eight other state-of-the-art models. We selected the MIT1003 and SID4VAM benchmarks for comparison of the quantitative results. These results are reported in Tabs. 2, 3, and 4. The superior performance, in terms of saliency prediction, was achieved by models based on biological/cognitive and Fourier/spectral foundations. Our model achieved stable and superior performance, in terms of different evaluation metrics, compared to other biological/cognitive- and Fourier/spectral-inspired models. However, saliency map prediction based on a convolutional neural network outperformed other models in natural scene images, as more images are used to train the neural network. Consequently, these cannot be compared to other models, as they are based more on statistical than neuroscientific principles. In this paper, we emphasize understanding saliency prediction from a neuroscience perspective, in order to further help us understand the mechanism of visual attention cognitive function. Furthermore, biological/cognitive- and Fourier/spectral-inspired saliency detection models were outperformed by deep learning approaches (ML_Net and DeepGazeII) in the SID4VAM dataset (see Tab. 4 and Fig. 13). As previously said, SID4VAM is a synthetic image database that is primarily used to psychophysically test the V1 properties, which is also why we stated that deep learning models refer more from statistics than neuroscience in the explanation of human visual attention mechanisms.

Methods	DNN	AUC_Judd	AUC_Borji	sAUC	NSS	SIM
ITT	B	0.674	0.655	0.610	0.629	0.291
WECSF	N	0.705	0.692	0.653	0.849	0.362
SR	N	0.708	0.683	0.638	0.791	0.329
AIM	N	0.706	0.696	0.639	0.780	0.282
BMS	N	0.684	0.637	0.576	0.729	0.346
CASD	N	0.747	0.731	0.651	0.977	0.350
DCTS	N	0.746	0.732	0.650	1.000	0.322
HFT	N	0.797	0.764	0.619	1.258	0.416
ICL	N	0.769	0.713	0.617	1.048	0.420
PFT	N	0.708	0.683	0.636	0.787	0.326
PQFT	N	0.643	0.530	0.519	0.459	0.292
QDCT	N	0.736	0.714	0.647	0.920	0.338
RARE	N	0.777	0.755	0.665	1.198	0.380
SIM	N	0.701	0.693	0.653	0.743	0.283
SUN	N	0.665	0.647	0.601	0.629	0.287
Achanta	N	0.534	0.526	0.526	0.174	0.240
SimpSal	N	0.735	0.721	0.610	0.892	0.337
Spratling	N	0.512	0.508	0.510	0.039	0.234
SIMgrouping	N	0.724	0.716	0.668	0.873	0.308
SeoMilanfar	N	0.710	0.688	0.633	0.808	0.351
ML_Net	Y	0.836	0.743	0.689	1.928	0.565
DeepGazeII	Y	0.886	0.837	0.779	2.483	0.527

Table 2: Quantitative scores of several models for the MIT1003 dataset. The baseline ITT model is shaded in blue and the proposed model is shown in green. The black bold scores indicate the best performance of the saliency prediction models. “N” indicates NO, “Y” indicates YES, and “B” indicates Baseline. The results of ML_Net and DeepGazeII models for the MIT1003 dataset are shown in pink, as this dataset was used to train ML_Net and DeepGazeII and, so, their results could not be compared with those of the other models.

4.2 Qualitative Comparison of the Proposed Model with Other State-of-the-Art Models

We qualitatively tested the proposed model using the MIT1003, MIT300, TORONTO, SID4VAM, and UCF Sports datasets. We also compared the model’s performance with those of other state-of-the-art saliency prediction models on the MIT1003, TORONTO, and SID4VAM datasets. Figs. 10, 11, 12, 13, and 14 illustrate the saliency map results

Methods	DNN	AUC_Judd	AUC_Borji	sAUC	NSS	SIM
ITT	B	0.700	0.679	0.641	0.816	0.317
WECSF	N	0.701	0.686	0.674	0.844	0.365
SR	N	0.744	0.722	0.683	1.019	0.343
AIM	N	0.727	0.718	0.664	0.885	0.356
SIM	N	0.754	0.744	0.707	0.951	0.361
SUN	N	0.674	0.653	0.613	0.656	0.285
HFT	N	0.820	0.792	0.659	1.548	0.522
ICL	N	0.792	0.737	0.652	1.245	0.532
PFT	N	0.742	0.717	0.684	1.001	0.339
CASD	N	0.780	0.764	0.688	1.237	0.364
PQFT	N	0.650	0.524	0.517	0.482	0.263
QDCT	N	0.769	0.748	0.691	1.174	0.354
RARE	N	0.806	0.774	0.693	1.514	0.402
Achanta	N	0.551	0.541	0.539	0.249	0.305
Simpsal	N	0.769	0.754	0.648	1.121	0.355
Spratling	N	0.508	0.503	0.509	0.015	0.242
SIMgrouping	N	0.769	0.760	0.710	1.090	0.326
SeoMilanfar	N	0.769	0.744	0.695	1.185	0.382
ML_Net	Y	0.823	0.803	0.750	1.824	0.536
DeepGazeII	Y	0.846	0.827	0.756	2.199	0.620

Table 3: Quantitative scores of several models for the TORONTO dataset. The baseline ITT model is shown in blue and the proposed model is shown in green. The black bold scores indicate the best performance of the saliency prediction models. The results of ML_Net and DeepGazeII for the TORONTO dataset are shown in pink, as this dataset was used to train ML_Net and DeepGazeII and, so, their results could not be compared with those of the other models.

Models	DNN	AUC_Judd	AUC_Borji	sAUC	CC	NSS	KL	SIM	IG
GT	B	0.943	0.882	0.860	1.000	4.204	0.000	1.000	2.802
Baseline-CG	B	0.703	0.697	0.525	0.281	1.577	0.722	0.372	-0.189
ITT	B	0.645	0.592	0.591	0.165	0.801	1.778	0.315	-0.104
WECSF	N	0.667	0.647	0.646	0.378	1.019	1.769	0.459	-1.508
AIM	N	0.572	0.566	0.560	0.118	0.515	14.96	0.216	-18.742
Achanta	N	0.505	0.513	0.513	0.060	0.334	8.431	0.117	-9.634
BMS	N	0.811	0.517	0.515	0.129	0.702	19.161	0.624	-24.258
CASD	N	0.737	0.673	0.663	0.429	2.124	2.659	0.397	-1.263
DCTS	N	0.732	0.725	0.715	0.440	2.191	1.442	0.377	0.363
HFT	N	0.780	0.753	0.697	0.561	2.364	1.424	0.458	0.406
ICL	N	0.742	0.716	0.630	0.344	1.189	1.974	0.391	-0.443
PFT	N	0.704	0.692	0.688	0.407	2.074	2.556	0.361	-1.230
PQFT	N	0.581	0.518	0.517	0.112	0.611	12.262	0.175	-15.074
QDCT	N	0.717	0.705	0.699	0.419	2.139	1.850	0.368	-0.213
SIM	N	0.648	0.638	0.628	0.181	0.744	1.799	0.340	-0.152
SR	N	0.747	0.695	0.689	0.423	2.087	1.508	0.414	0.354
SUN	N	0.545	0.536	0.535	0.086	0.403	17.387	0.155	-22.268
Simpsal	N	0.753	0.740	0.661	0.370	1.380	1.461	0.393	0.323
Spratling	N	0.535	0.527	0.534	0.030	0.176	17.801	0.147	-22.890
SIMgrouping	N	0.649	0.638	0.638	0.191	0.866	1.925	0.350	-0.338
SeoMilanfar	N	0.703	0.692	0.698	0.246	1.181	2.696	0.337	-1.400
ML_Net	Y	0.600	0.593	0.501	0.118	0.341	7.529	0.370	-2.153
DeepGazeII	Y	0.645	0.581	0.475	0.103	0.555	2.450	0.274	-1.128

Table 4: Quantitative scores of several models for the SID4VAM dataset. The baseline ITT model is shown in blue and the proposed model is shown in green. The black bold scores indicate the best performance of the saliency prediction models. The Fourier/spectral-inspired models had the best prediction scores, compared to the other start-of-the-art non-neural network (and even deep neural network) models on the SID4VAM dataset. The results of ML_Net and DeepGazeII on the SID4VAM dataset are shown in pink, as this dataset was used to train them, and their results could not be compared with those of the other models.

obtained when the proposed model and other state-of-the-art models were applied to sample images drawn from the studied datasets. The performance of each of saliency prediction model was evaluated through AUC and PR curves, as shown in Fig. 15. We can see that the proposed model could predict most of the salient objects in the given images. Furthermore, the proposed model could successfully detect the orientation, boundary, and pop-out function when the model was applied to the SID4VAM dataset. In summary, our proposed biological/Fourier/spectral inspired-saliency prediction model achieved superior and stable performance on natural images, psychophysical synthetic images, and dynamic scenes, compared with other existing models.

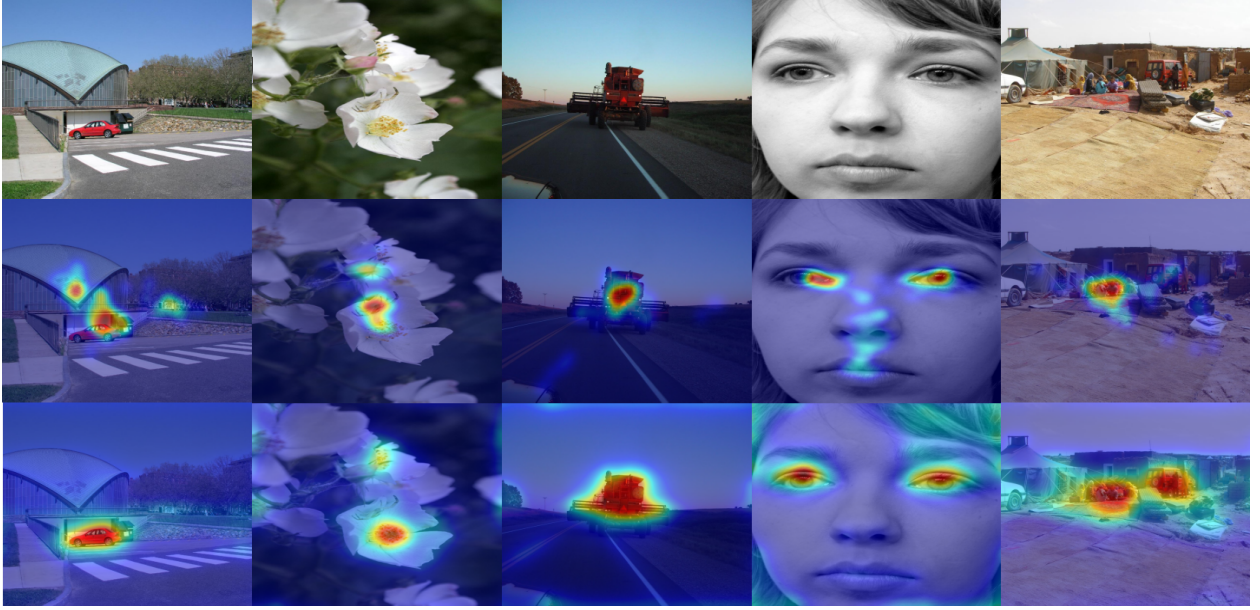


Figure 10: Performance evaluation on the MIT1003 dataset. The first row shows color images, the second row shows ground-truth saliency maps, and the last row shows the proposed model’s predicted saliency maps, respectively.

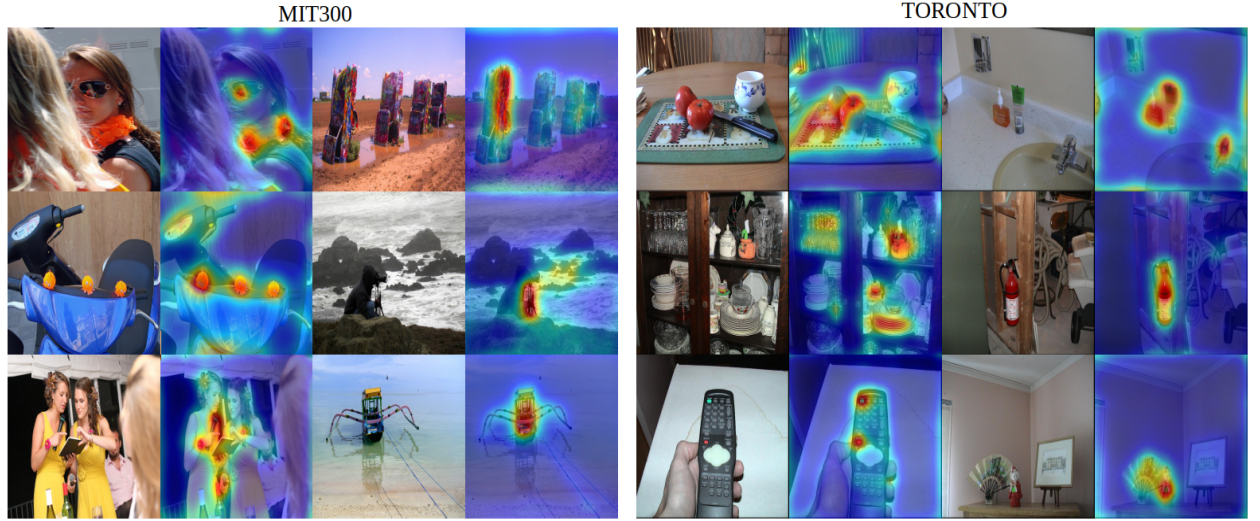


Figure 11: Left: Performance evaluation on the MIT300 dataset. The first and third columns are color images. The second and fourth columns are the proposed model’s predicted saliency maps. Right: Performance evaluation on the TORONTO dataset. The first and third columns are color images. The second and fourth columns are the proposed model’s predicted saliency maps.

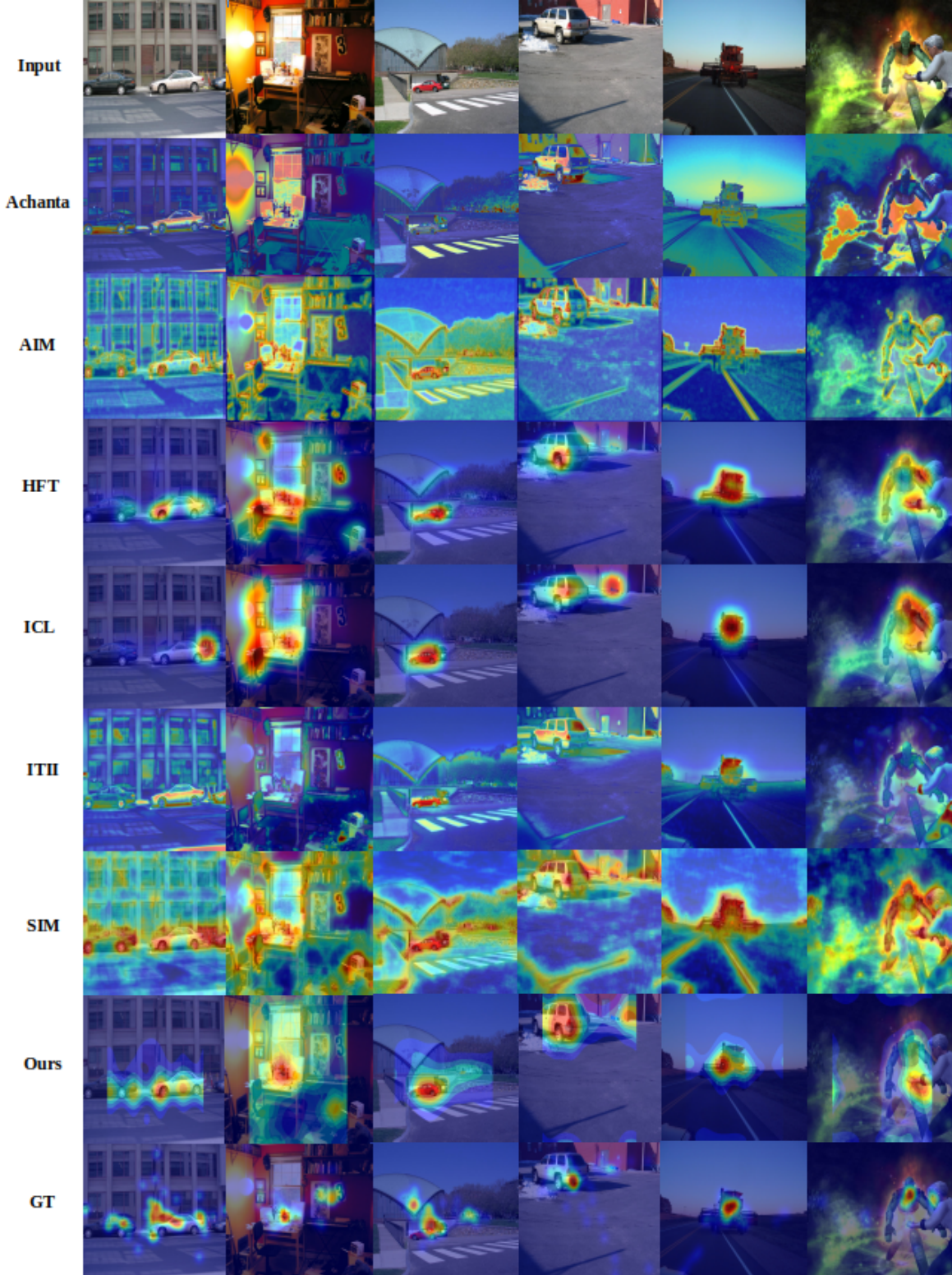


Figure 12: Qualitative saliency prediction results on the MIT1003 dataset with different models. The first row shows six stimuli images selected from the MIT1003 dataset. The rows below show the predicted saliency maps obtained with Achanta, AIM, HFT, ICL, ITII, SIM, and the proposed model, as well as the ground-truth (GT) saliency, with artificial color for better visualization.

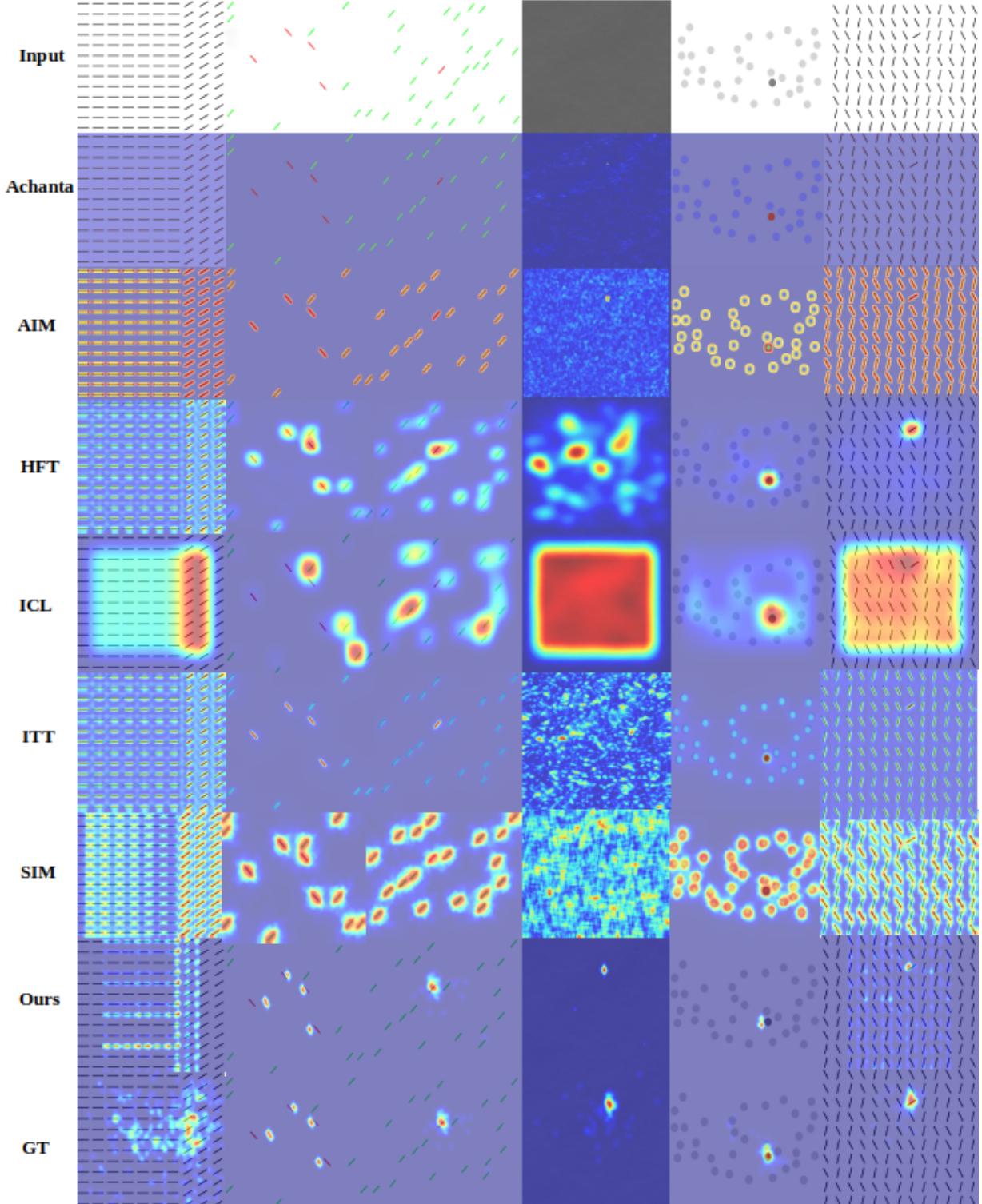


Figure 13: Qualitative saliency prediction results on the SID4VAM dataset with different models. The first row shows six stimuli images selected from the SID4VAM dataset. The rows beneath show the saliency prediction results obtained with Achanta, AIM, HFT, ICL, ITT, SIM, and the proposed model, as well as the ground truth (GT) saliency, with artificial color for better visualization. The proposed model can be successfully applied to explain the “pop-out” effects in the visual search.

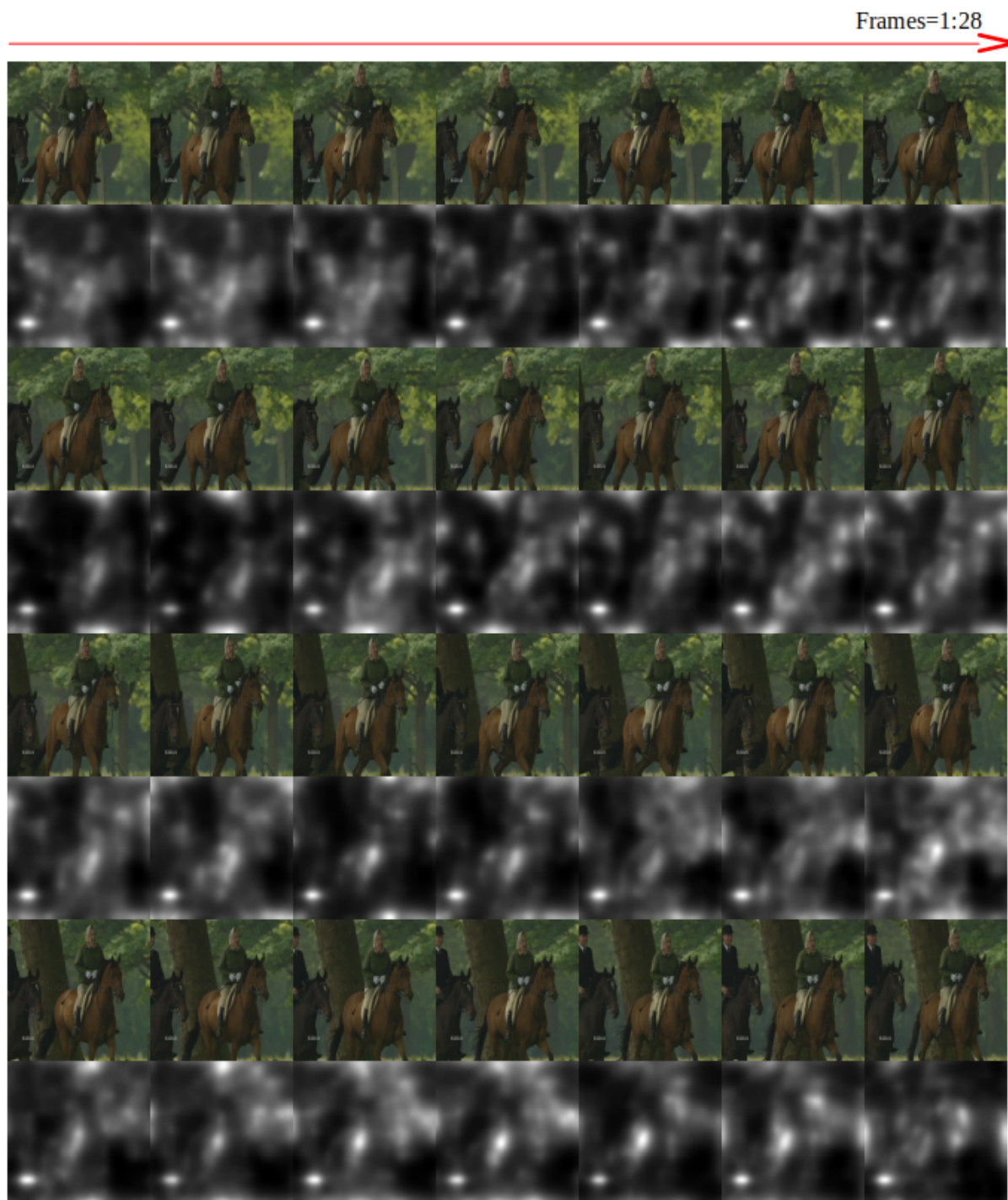


Figure 14: Dynamic saliency prediction. For these sample frames from the UCF Sports Action dataset, the model clearly produced better results and perfectly captured the text information on the bottom-left.

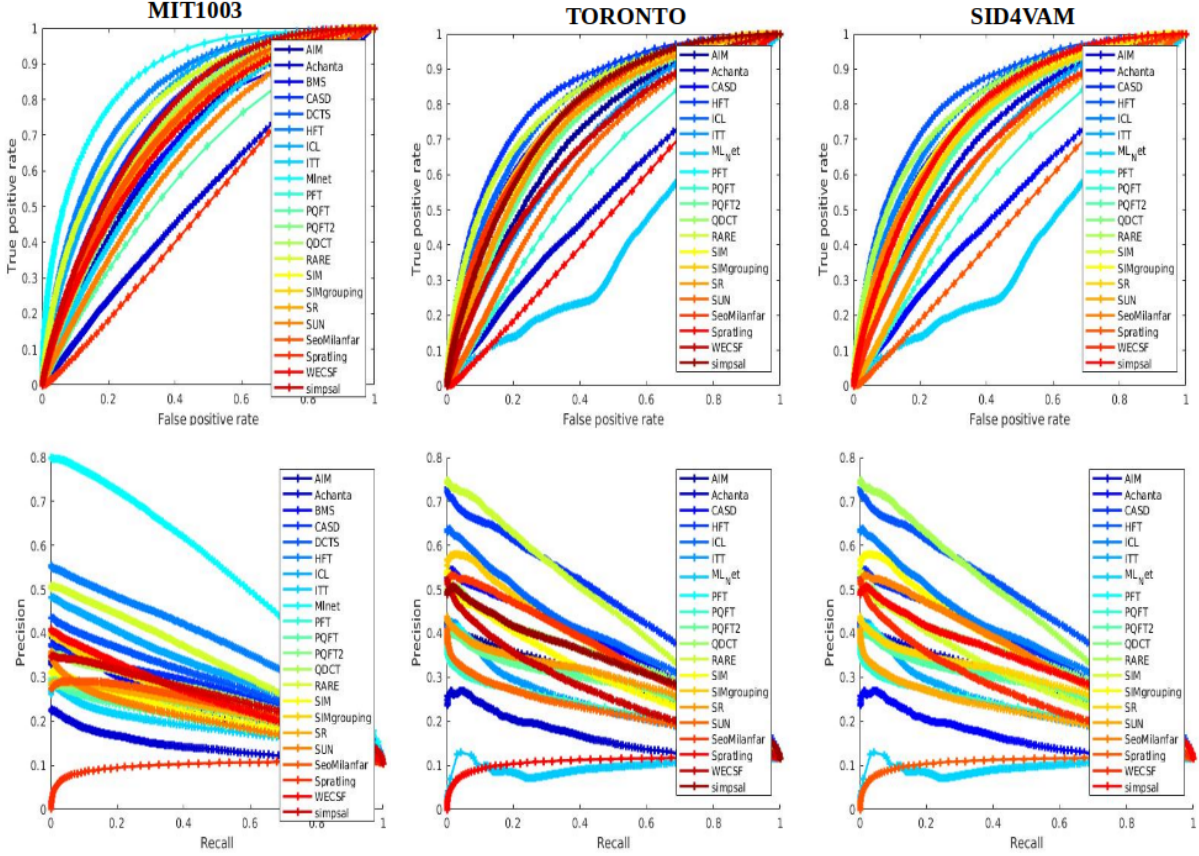


Figure 15: Comparison of the area under the ROC curve (AUC) and PR curves, with different thresholds between our method and other state-of-the-art methods on three benchmark datasets.

5 Discussion

Saliency modeling has become a hot research topic in the computer vision and neuroscience fields. Therefore, researchers have attempted to use new architectures, which have not yet sufficiently improved model performance. Instead, we should investigate how humans perceive scenes; what guides their attention is critical. In this article, I discussed several ways to go beyond the capabilities of such models.

First, it is necessary to understand the cognitive attention mechanism. Visual attention is a selective cognitive process that allows us to deal effectively with this issue, by choosing important information and filtering out irrelevant information. In saliency prediction studies, spatial attention plays a significant role in discrimination and appearance tasks, being affected by the spatial resolution and contrast sensitivity. Exploring the neural mechanisms of visual attention can help us to develop better and more accurate saliency prediction models. In contrast, better saliency prediction models also can help us to understand the cognitive process of visual attention in the brain. Second, we need multi-model and multi-label datasets to evaluate saliency prediction model performance. The domain datasets used to assess the saliency prediction model were the MIT Saliency benchmark datasets. As mentioned previously, the saliency prediction model should not only achieve higher accuracy on natural scene images, but also on psychophysical synthetic images (e.g., SID4VAM). This could help to improve the model architecture and help us to understand the cognitive attention process. Third, we provided comprehensive experimental results, showing that our method consistently achieved stable and superior performances in comparison to other state-of-the-art methods. It is worth noting that we measured saliency using biologically inspired visual model estimation. Our proposed saliency prediction model takes more neuroscience concepts into account, rather than probabilistic/statistical concepts. Furthermore, the proposed model has few parameters, which were largely set and fixed for all experiments. The use of wavelet energy maps and opponent CSFs as features was one of the most critical factors that made the proposed method more efficient. Furthermore, our comprehensive experimental results indicated that the proposed saliency prediction measure derived from a local

image energy estimator is much more effective and straightforward than other existing methods. Although our method was constructed entirely on biologically inspired computational principles, the resulting model structure exhibited considerable agreement with the fixation behavior of the human visual system.

6 Conclusions

In this study, a computational psychophysical visual saliency prediction model inspired by a low-level human visual pathway was proposed. The model includes color opponent channels, wavelet transform, wavelet energy map, and contrast sensitivity functions, in order to predict the saliency map. The model was evaluated by classical benchmark datasets, and achieved stable and good performance, in terms of visual saliency prediction, compared with the baseline model. Furthermore, we found that models based on deep neural networks out-performed ours, in terms of natural image salience prediction, but under-performed for psychophysical synthetic images. In contrast, Fourier/spectral-inspired models had the opposite effect, as Fourier/spectral-inspired models simulate optical neural processing from the retina to the V1; however, deep neural networks take statistics into account more than low-level vision system functioning. Finally, we also extended our model to spatial-temporal saliency prediction, and it was capable of capturing the most significant feature in the videos.

7 Acknowledgments

I thank the anonymous reviewers, whose suggestions helped to improve and clarify this manuscript. This research received no external funding.

8 Conflicts of Interest

The author declares no conflicts of interest.

9 Abbreviations

HSV	Human Vision System
V1	Primary Visual Cortex
ICL	Incremental Coding Length
CNN	Convolution Neural Network
DNN	Deep Neural Network
WT	Wavelet Transform
IWT	Inverse Wavelet Transform
AUC	Area Under the ROC Curve
NSS	Normalized Scanpath Saliency
CC	Pearson's Correlation Coefficient
SIM	Similarity or Histogram Intersection
IG	Information Gain
KL	Kullback–Leibler divergence
CSF	Contrast Sensitivity Function
FT	Fourier Transform
DWT	Discrete Wavelet Transform
IDWT	Inverse Discrete Wavelet Transform
LGN	Lateral Geniculate Nucleus
GT	Ground Truth

References

- R. Achanta, S. Hemami, F. Estrada, and S. Süsstrunk. Frequency-tuned salient region detection. *Proceedings of the IEEE Conference on Computer Vision Pattern Recognition (CVPR)*, 06 2009.
- H. Barlow. Sensory mechanisms, the reduction of redundancy, and intelligence. *Proc. of the Nat. Phys. Lab. Symposium on the Mechanization of Thought Process*, (10):535–539, 1959.
- H. Barlow. *Vision: Coding and Efficiency*, chapter A theory about the functional role and synaptic mechanism of visual aftereffects. Cambridge Univ. Press, Cambridge, UK, 1990.

- D. Berga, X. R. Fdez-Vidal, X. Otazu, and X. M. Pardo. Sid4vam: A benchmark dataset with synthetic images for visual attention modeling. *2019 IEEE/CVF International Conference on Computer Vision (ICCV)*, pages 8788–8797, 2019.
- A. Borji. Saliency prediction in the deep learning era: Successes and limitations. *IEEE transactions on pattern analysis and machine intelligence*, PP, 08 2019.
- A. Borji, H. Rezazadegan Tavakoli, D. Sihite, and L. Itti. Analysis of scores, datasets, and models in visual saliency prediction. pages 921–928, 12 2013.
- M. Brill. *Trichromatic Theory*, pages 827–829. 01 2014. ISBN 978-0-387-30771-8.
- N. D. B. Bruce and J. K. Tsotsos. Saliency based on information maximization. In *Proceedings of the 18th International Conference on Neural Information Processing Systems, NIPS’05*, page 155–162, Cambridge, MA, USA, 2005. MIT Press.
- M. Butz. Toward a cognitive sequence learner: Hierarchy, self-organization, and top-down bottom-up interaction. 04 2004.
- Z. Bylinskii, T. Judd, A. Oliva, A. Torralba, and F. Durand. What do different evaluation metrics tell us about saliency models? *arXiv preprint arXiv:1604.03605*, 2016.
- M. Cornia, L. Baraldi, G. Serra, and R. Cucchiara. A deep multi-level network for saliency prediction. 09 2016.
- M. Emami and L. Hoberock. Selection of a best metric and evaluation of bottom-up visual saliency models. *Image and Vision Computing*, 31:796–808, 10 2013.
- U. Engelke, H. Liu, J. Wang, P. Le Callet, I. Heynderickx, H.-J. Zepernick, and A. Maeder. A comparative study of fixation density maps. *IEEE transactions on image processing : a publication of the IEEE Signal Processing Society*, 11 2012.
- M. Feng. Evaluation toolbox for salient object detection. https://github.com/ArcherFMY/sal_eval_toolbox, 2018.
- G. Finlayson, M. Drew, and B. Funt. Color constancy: Enhancing von kries adaptation via sensor transformations. *Proc SPIE*, 1913, 09 1993.
- G. D. Finlayson, A. Alsam, and S. D. Hordley. Local linear models for improved von kries adaptation. In *The Tenth Color Imaging Conference: Color Science and Engineering Systems, Technologies, Applications, CIC 2002, Scottsdale, Arizona, USA, November 12-15, 2002*, pages 139–144. IS&T - The Society for Imaging Science and Technology, 2002.
- S. Goferman, L. Zelnik-Manor, and A. Tal. Context-aware saliency detection. pages 2376 – 2383, 07 2010.
- C. Guo, Q. Ma, and L. Zhang. Spatio-temporal saliency detection using phase spectrum of quaternion fourier transform. 06 2008.
- A. Haar. Zur theorie der orthogonalen funktionensysteme. (zweite mitteilung). *Mathematische Annalen*, 71:38–53, 1912. URL <http://eudml.org/doc/158516>.
- J. Harel. A saliency implementation in matlab. <http://www.klab.caltech.edu/~harel/share/gbvs.php>, 2012.
- X. Hou and L. Zhang. Saliency detection: A spectral residual approach. volume 2007, 06 2007.
- X. Hou and L. Zhang. Dynamic visual attention: Searching for coding length increments. volume 21, pages 681–688, 01 2008.
- X. Hou, J. Harel, and C. Koch. Image signature: Highlighting sparse salient regions. *IEEE transactions on pattern analysis and machine intelligence*, 34, 07 2011.
- L. Hurvich and D. Jameson. An opponent-process theory of color vision. *Psychological Review*, 64:384–404, 12 1957.
- N. imamoğlu, W. Lin, and Y. Fang. A saliency detection model using low-level features based on wavelet transform. *IEEE Transactions on Multimedia*, 15:96–105, 01 2013.
- L. Itti. *Models of Bottom-Up and Top-Down Visual Attention*. PhD thesis, Pasadena, California, Jan 2000.
- L. Itti, C. Koch, and E. Niebur. A model of saliency-based visual attention for rapid scene analysis. *Pattern Analysis and Machine Intelligence, IEEE Transactions on*, 20:1254 – 1259, 12 1998.
- T. Jost, N. Ouerhani, R. Wartburg, R. Müri, and H. Hügli. Assessing the contribution of color in visual attention. *comput. vis. image und.* 100, 107-123. *Computer Vision and Image Understanding*, 100:107–123, 10 2005.
- T. Judd, F. Durand, and A. Torralba. A benchmark of computational models of saliency to predict human fixations. In *MIT Technical Report*, 2012.
- J. Krauskopf and K. Gegenfurtner. Color discrimination and adaptation. *Vision research*, 32:2165–75, 12 1992.

- S. Kruthiventi, V. Gudisa, J. Dholakiya, and R. Babu. Saliency unified: A deep architecture for simultaneous eye fixation prediction and salient object segmentation. pages 5781–5790, 06 2016.
- M. Kümmerer, T. S. A. Wallis, and M. Bethge. Deepgaze II: reading fixations from deep features trained on object recognition. *CoRR*, abs/1610.01563, 2016. URL <http://arxiv.org/abs/1610.01563>.
- M. Kümmerer, T. Wallis, and M. Bethge. Information-theoretic model comparison unifies saliency metrics. *Proceedings of the National Academy of Sciences*, 112:201510393, 12 2015a.
- M. Kümmerer, T. Wallis, and M. Bethge. Information-theoretic model comparison unifies saliency metrics. *Proceedings of the National Academy of Sciences*, 112:201510393, 12 2015b.
- J. li, M. Levine, X. An, X. Xu, and H. He. Visual saliency based on scale-space analysis in the frequency domain. *IEEE Transactions on Pattern Analysis and Machine Intelligence*, 35:996–1010, 11 2012.
- A. Louis, P. Maass, and A. Rieder. *Wavelets: Theory and Applications*. 01 1997. ISBN 978-0-471-96792-7.
- J. Mannos and D. Sakrison. The effects of a visual fidelity criterion of the encoding of images. *IEEE Transactions on Information Theory*, 20(4):525–536, 1974.
- D. Mercy. A review of automatic gain control theory. *Radio and Electronic Engineer*, 51, 01 1981.
- K. Mullen. The contrast sensitivity of human color vision to red-green and blue-yellow chromatic gratings. *The Journal of physiology*, 359:381–400, 03 1985.
- N. Murray, M. Vanrell, X. Otazu, and C. A. Párraga. Saliency estimation using a non-parametric low-level vision model. pages 433–440, 06 2011.
- N. Murray, M. Vanrell, X. Otazu, and C. A. Párraga. Low-level spatiochromatic grouping for saliency estimation. *IEEE transactions on pattern analysis and machine intelligence*, 35:2810–6, 11 2013.
- X. Otazu, C. A. Párraga, and M. Vanrell. Toward a unified chromatic induction model. *Journal of vision*, 10:5, 10 2010.
- B. Pinna, A. Reeves, J. Koenderink, A. Doorn, and K. Deiana. A new principle of figure-ground segregation: The accentuation. *Vision research*, 143, 12 2017.
- N. Riche, M. Mancas, B. Gosselin, and T. Dutoit. Rare: A new bottom-up saliency model. 10 2012.
- N. Riche, M. Duvinage, M. Mancas, B. Gosselin, and T. Dutoit. Saliency and human fixations: State-of-the-art and study of comparison metrics. 12 2013.
- B. Schauerte and R. Stiefelhagen. Quaternion-based spectral saliency detection for eye fixation prediction. pages 116–129, 10 2012. ISBN 978-3-642-33708-6.
- A. Selvaraj and N. Shebiah. Object recognition using wavelet based salient points. *The Open Signal Processing Journal*, 2:14–20, 09 2009.
- H. Seo and P. Milanfar. Static and space-time visual saliency detection by self-resemblance. *Journal of vision*, 9: 15.1–27, 11 2009.
- R. Shapley and M. Hawken. Color in the cortex: Single- and double-opponent cells. *Vision research*, 51:701–17, 02 2011.
- M. Spratling. Predictive coding as a model of the v1 saliency map hypothesis. *Neural networks : the official journal of the International Neural Network Society*, 26:7–28, 10 2011.
- M. Spratling. A review of predictive coding algorithms. *Brain and Cognition*, 112, 01 2016.
- Y. Sun and R. Fisher. Object-based visual attention for computer vision. *Artificial Intelligence*, 146:77–123, 05 2003.
- A. Treisman and G. Gelade. A feature-integration theory of attention. *Cognitive psychology*, 12:97–136, 02 1980.
- D. Wang, A. Kristjansson, and K. Nakayama. Efficient visual search without top-down or bottom-up guidance. *Perception & psychophysics*, 67:239–53, 03 2005.
- A. Watson and A. Ahumada. The spatial standard observer. *Journal of Vision - J VISION*, 4:51–51, 01 2010.
- A. Watson and J. Malo. Video quality measures based on the standard spatial observer. volume 3, pages III–41, 02 2002. ISBN 0-7803-7622-6.
- N. Wilming, T. Betz, T. Kietzmann, and P. König. Measures and limits of models of fixation selection. *PloS one*, 6: e24038, 09 2011.
- J. Zhang and S. Sclaroff. Saliency detection: A boolean map approach. pages 153–160, 12 2013.
- L. Zhang, M. Tong, T. Marks, H. Shan, and G. Cottrell. Sun: A bayesian framework for saliency using nature statistics. *Journal of vision*, 8:32.1–20, 02 2008.
- L. Zhaoping. A neural model of contour integration in the primary visual cortex. *Neural computation*, 10:903–40, 05 1998.